*electronics*

MDPI

*Article*

# Design and Analysis of a Superconducting Homopolar Inductor Machine for Aerospace Application

**Jiabao Wang [1], Chao Guo [2,*], Wanyu Zhou [1] and Qin Wan [1]**

[1] College of Electrical and Information Engineering, Hunan Institute of Engineering, Xiangtan 411104, China; wjb19523@hnie.edu.cn (J.W.); zhouwanyu@stu.hnie.edu.cn (W.Z.); wanqin@hnie.edu.cn (Q.W.)
[2] College of Electrical Engineering, Hunan Mechanical Electrical Polytechnic, Changsha 410151, China
* Correspondence: 17023@hnie.edu.cn

**Abstract:** The electrically excited homopolar inductor machine has a static excitation coil as well as a robust rotor, which makes it attractive in the field of high-speed superconducting machines. This paper designed and analyzed a megawatt class superconducting homopolar inductor machine for aerospace application. To improve the power density, a mass-reduced rotor structure is proposed. Firstly, the main structure parameters of the superconducting homopolar inductor machine are derived based on the required power and speed. Secondly, the electromagnetic performance of the superconducting homopolar inductor machine is analyzed based on the finite element method. Thirdly, a mass-reduced rotor is proposed to improve its power density. The structural performance of the rotor and the electromagnetic performance of the superconducting homopolar inductor machine before and after rotor-mass reduction are evaluated. Compared with the initial rotor, the mass of the mass-reduced rotor is reduced from 66.56 kg to 50.02 kg, which increases the power density by 14.3%. The result shows that a superconducting homopolar inductor machine with a mass-reduced rotor can effectively improve its power density without affecting its output power.

**Keywords:** superconducting machine; homopolar inductor machine; aerospace

check for updates

**Citation:** Wang, J.; Guo, C.; Zhou, W.; Wan, Q. Design and Analysis of a Superconducting Homopolar Inductor Machine for Aerospace Application. *Electronics* **2024**, *13*, 2830. https://doi.org/10.3390/electronics13142830

Academic Editor: Ahmed Abu-Siada

Received: 26 May 2024
Revised: 18 June 2024
Accepted: 24 June 2024
Published: 18 July 2024

**Copyright:** © 2024 by the authors. Licensee MDPI, Basel, Switzerland. This article is an open access article distributed under the terms and conditions of the Creative Commons Attribution (CC BY) license (https://creativecommons.org/licenses/by/4.0/).

## 1. Introduction

In recent years, zero-emission all-electric aircraft have attracted a lot of attention [1]. Electric motors play a key role in airborne power systems as energy conversion equipment. The output power of a motor is proportional to its electromagnetic load and rotation speed. Thus, to achieve high power density, the design of motor pursues higher electromagnetic load and higher rotational speed at present. The commonly used permanent magnet motor has a high power density, but the reliability of its permanent magnet would be greatly threatened under the extreme working conditions of aviation electromechanical systems [2].

With the development of superconducting technology, the miniaturized, lightweight and high-power-density superconducting motor has become a research hotspot. Due to its higher reliability, the partially superconducting motor with a superconducting excitation coil has a wider range of application compared to the fully superconducting motor [3]. The superconducting excitation coil allows a large magnetic load to be applied to the motor, overcoming the disadvantages of conventional electrically excited synchronous motors. However, for rotor superconducting synchronous motors, the design of the cooling device is complicated and its reliability is reduced due to the excitation coil being in a state of high-speed rotation [4,5]. Thus, synchronous motors with superconducting stator static excitation have attracted much attention in the aerospace industry due to their high reliability and the low complexity of their cooling systems [6]. In [7], a new stator high-temperature superconducting field-modulated machine with a simple structure was proposed. A stator flux modulation machine was proposed in [2], which realized the static excitation of the superconducting coil. However, the mismatch between the excitation

field and the armature fundamental field leads to serious AC copper losses; as a result, the efficiency of the machine is reduced. A superconducting vernier reluctance motor was proposed in [8], but it is still a challenge to cool the armature and the superconducting coil located on the stator side.

The superconducting homopolar induction machine (SHIM) stands out among many superconducting motors for its advantages of static excitation, simple structure and high-speed operation [9,10]. Several studies have presented the conceptual design of the SHIM [11,12]. In [13], a 10 MW class superconducting homopolar generator was presented for wind turbines. In [14], a 2 MW, 25000 rpm SHIM using ReBCO field coils was proposed for aircraft propulsion to reduce development and construction time and cost. In [15], to ensure the safe operation and improve the performance of SHIM, the superconducting coil in SIM was designed considering the critical current reduction in local turn. However, these studies did not deeply explore how to improve the power density of the SHIM. Other research focused on achieving high rotational speed of SHIM [16,17]. In [18], to suppress the alternating field acting on the superconducting coil in SHIM, a combined method using two sets of U-shaped armature winding and an L-shaped flux diverter was proposed. In addition, the loss of the superconducting magnet in SHIM is analyzed and calculated in [19]. However, these studies lack analysis into the reliability of SHIM in high-speed operations, especially the rotor.

To better meet the needs of future aerospace motors, SHIM is taken as a research object, and a 1 MW, 21,000 rpm SHIM is designed in this paper. The electromagnetic and structural properties of SHIM are analyzed through the finite element method (FEM). To reduce the weight of the SHIM, a rotor weight reduction structure is proposed. The rest of this paper is arranged as follows: In Section 2, the topology of the SHIM and its operating principle are introduced. In Section 3, the main dimensions of the SHIM and the mathematical model of its basic electromagnetic parameters are modeled. Then, the electromagnetic performance of SHIM is evaluated using the FEM. In Section 4, a mass-reduced rotor is proposed to improve the power density of SHIM, and the electromagnetic performance of the SHIM before and after mass reduction is compared. The conclusions of this paper are drawn in Section 5.

## 2. Topology and Operation Principle

The structure of the SHIM is shown in Figure 1. The shell is made of material with good magnetic permeability and is located on the outermost side. Silicon steel sheets are laminated along the axial direction to form the slotless stator cores. The core mass is reduced through drilling the stator cores [20]. A set of armature winding is placed on the inner wall of the stator. The rotor of the SHIM is forged from a single piece of high-strength alloy steel, which allows it to operate at extremely high rotational speeds. The rotor teeth are evenly distributed on the left and right sides of the rotor, and the rotor tooth axes on both sides differ in space by $\pi$ electrical degree.

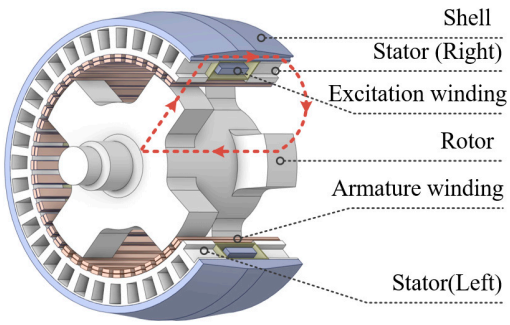



**Figure 1.** Topology of superconducting homopolar inductor machine.

To pursue a higher magnetic load and reduce excitation loss, the conventional copper excitation winding is replaced by the superconducting coil that is stationarily installed between the left and right stator cores. Figure 2 shows the two-dimensional cross-section view of the cryostat. The static excitation of the superconducting coil avoids the introduction of rotary sealing and cooling, which improves the reliability of the system.

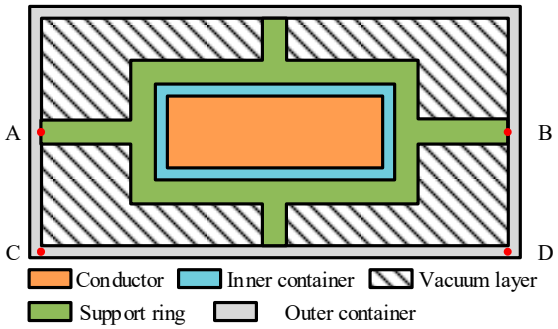



**Figure 2.** Two-dimensional cross-section of the super-conducting winding.

The flux generated by the superconducting excitation winding is shown by the red dotted line in Figure 1. The air-gap flux density has AC components due to the cogging effect of the rotor. As the rotor rotates, a back electromotive force (EMF) is generated on the armature winding.

## 3. Electromagnetic Performance Design

### *3.1. Calculation of Main Structure Parameters*

The rated power $P$ of SHIM can be expressed as follows:

$$P = m_1 EI \tag{1}$$

The back EMF $E$ of SHIM can be expressed as follows:

$$E = 4k_{Nm} f N k_{dp} \Phi \tag{2}$$

The flux per pole is expressed as follows:

$$\Phi = B_{\max} \alpha_\delta \tau l_{ef} \tag{3}$$

Combining (1) to (3), the relationship between the main dimensions of SHIM can be expressed as follows [21]:

$$\frac{D2lefn}{P} = \frac{6.1}{\alpha_\delta k_{Nm} k_{dp} B_{\max} A} \tag{4}$$

Under the premise of ignoring the saturation, the amplitude of the air-gap flux density can be expressed as follows:

$$B_{\max} = F_{gap} \Lambda_{\max} = N_f i_f \mu_0 / (2 g_{\min}) \tag{5}$$

It can be seen from (4) and (5) that when the rated power of the SHIM is constant, the effective length and diameter of the armature winding are directly related to the line load $A$ and magnetic load $B_{\max}$. The larger the product of $A$ and $B_{\max}$, the smaller the volume of the SHIM. In addition, the ampere-turns of the excitation winding can be determined according to the given magnetic load and the minimum length of the physical air gap.

### *3.2. Calculation of Electromagnetic Parameters*

The calculation of electromagnetic parameters needs to first obtain the mathematical model of the no-load air-gap flux density. The two-dimensional expanded view of the rotor

along the circumference is given in Figure 3. Since the toothless stator is adopted in SHIM, only the specific permeability function on the rotor side needs to be considered.

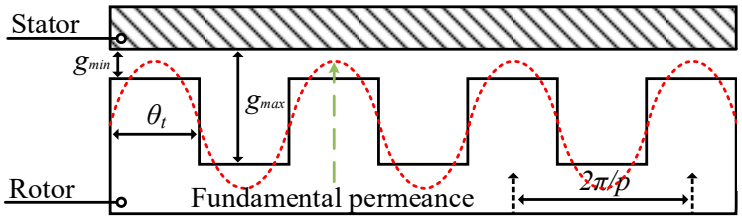



**Figure 3.** Two-dimensional expanded view of the rotor along the circumference.

The specific permeability functions of the air gaps on the left and right sides can be, respectively, expressed as follows [22]:

$$\begin{cases} \Lambda_L(\theta - \theta_r) = \sum_0^\infty \Lambda_m \cos mp(\theta - \theta_r) \\ \Lambda_R(\theta - \theta_r) = \sum_0^\infty \Lambda_m \cos mp(\theta - \theta_r - \frac{\pi}{p}) \end{cases} \tag{6}$$

Then, the open-circuit air-gap flux density on the left and right sides can be expressed as follows:

$$\begin{cases} B_L(\theta - \theta_r) = F_{gap} \sum_0^\infty \Lambda_m \cos mp(\theta - \theta_r) \\ B_R(\theta - \theta_r) = -F_{gap} \sum_0^\infty \Lambda_m \cos mp(\theta - \theta_r - \frac{\pi}{p}) \end{cases} \tag{7}$$

Based on the idea of space overlay method [23], the composite air-gap flux density ($B_C$) is expressed as

$$B_c(\theta, \theta_r) = B_L(\theta, \theta_r) + B_R(\theta, \theta_r) \tag{8}$$

The open-circuit flux linkage is represented as follows [24]:

$$\lambda_{i,j,k}(\theta r) = \frac{D}{2} \int_0^{L_{ef}} \int_0^{2\pi} N_{i,j,k}(\theta) B_c(\theta, \theta_r) d\theta dl \tag{9}$$

The back EMF of SHIM is expressed as follows [24]:

$$e_{i,j,k}(\theta_r) = \frac{d\lambda_{i,j,k}(\theta_r)}{d\theta_r} \frac{d\theta_r}{dt} = \omega_{mec} \frac{d\lambda_{i,j,k}(\theta_r)}{d\theta_r} \tag{10}$$

The torque of SHIM can be expressed by the product of back EMF and phase current as shown below [25], and in (11).

$$T_{elec} = P/\omega_{mec} = (e_a i_a + e_b i_b + e_c i_c)/\omega_{mec} \tag{11}$$

### *3.3. Numerical Analysis of Electromagnetic*

Based on the main dimensional relationship of the SHIM, a SHIM with the power of one megawatt is designed, and its no-load and load performance are evaluated by FEM. The detailed design process for the SHIM is given in [15,26]. The materials of each component and the main parameters of SHIM are shown in Tables 1 and 2. It is worth noting that the saturation magnetic density of the 1J22 is 2.4 T [27], and higher saturation magnetic density can make the magnetic load of the SHIM designed higher. In addition, combined with the advantages of superconducting field winding, the power density of the machine can be further improved.

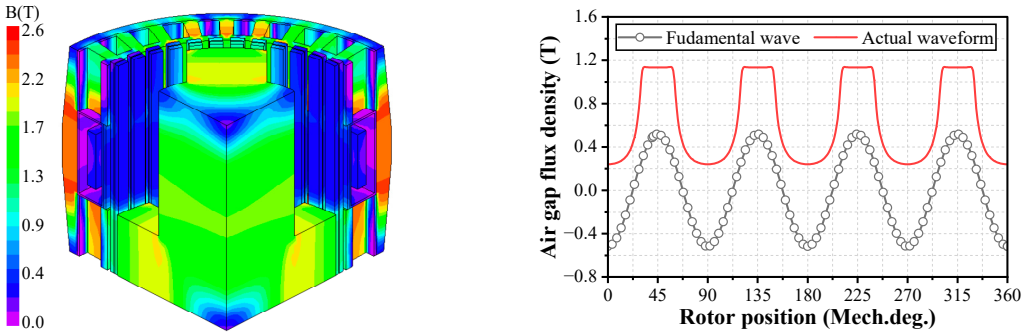
**Table 1.** Material and mass of each component.

| Components | Materials | Mass (kg) |
|---|---|---|
| Stator | 1J22 | 27.32 |
| Rotor | 40Cr | 66.56 |
| Shell | 1J22 | 35.36 |
| Armature winding | Litz wire | 12.32 |

**Table 2.** Main parameters of SHIM.

| Parameters (Unit) | Value |
|---|---|
| Inner diameter of stator yoke (mm) | 316 |
| Outer radius of rotor (mm) | 145 |
| Effective length of the rotor (mm) | 130 |
| Pole-pairs (-) | 4 |
| Coil pitch (-) | 5 |
| Synchronous speed (rpm) | 21,000 |
| Thickness of stator yoke (mm) | 40 |
| Rotor slot depth (mm) | 55 |
| Physical air-gap length (mm) | 13 |
| Virtual slots of the stator (-) | 48 |
| Ampere-turns of exciting winding (AT) | 30,000 |
| Rated power (kW) | 1000 |

The no-load magnetic field distribution and air-gap flux density of SHIM under rated excitation conditions are shown in Figure 4. The maximum magnetic density in the shell is 2.48 T, the amplitude of the air-gap flux density is 1.13 T, and the fundamental waveform amplitude is 0.52 T. The back EMF and its amplitude spectrum of the SHIM in the no-load state are given in Figure 5. The toothless stator and the short-pitch armature winding make the back EMF have good sinusoidal property in one electrical cycle.




(**a**) (**b**)

**Figure 4.** The static magnetic field flux density cloud diagram of SHIM and the air-gap flux density on one side of the air gap. (**a**) Magnetic field flux density cloud diagram. (**b**) Air-gap flux density.

The distribution of magnetic field around the superconducting coil is given in Figure 6, where AB is the distance from point A to point B in Figure 2. CD has a similar meaning to AB. Because the excitation flux needs to be closed axially through the rotor, the axial magnetic field at the bottom position of the excitation window (CD) is larger than that at the middle position (AB). Conversely, the radial flux density amplitude at CD is smaller than that at AB.

The output torque and power waveforms of SHIM are shown in Figure 7. In the rated state, the output power is one megawatt, and the torque is about 455 Nm.

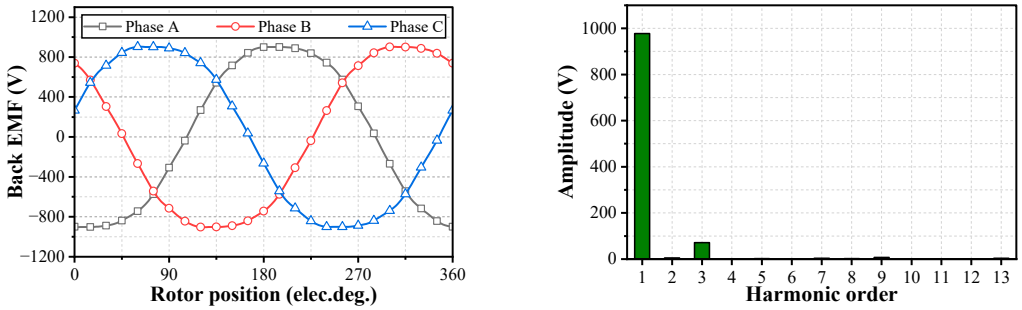



**Figure 5.** Phase back EMF and its amplitude spectrum. (**a**) Waveform of back EMF. (**b**) Amplitude spectrum.

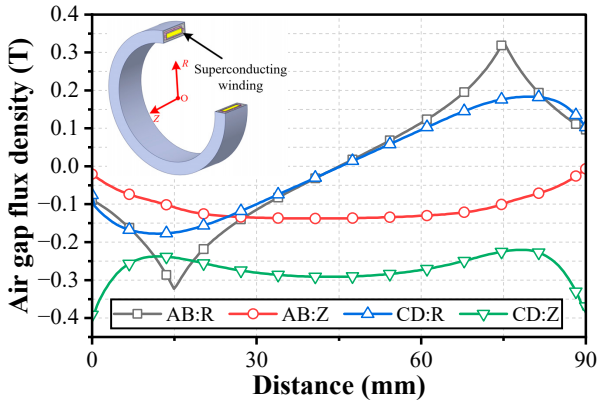



**Figure 6.** Magnetic field distribution around the superconducting coil.

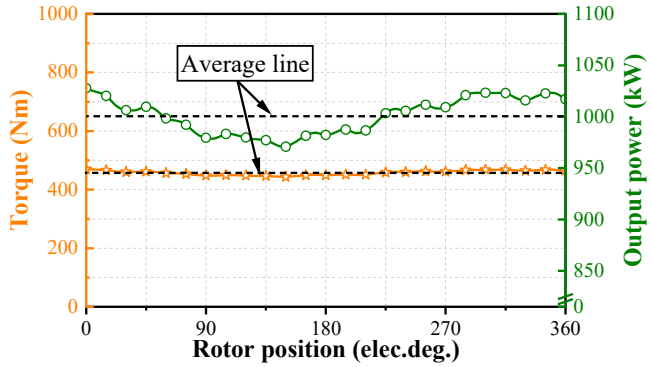



**Figure 7.** Output torque and power waveforms.

## 4. Mechanical Performance

For a rotor rotating at high speed, its rotational speed is limited by the strength of material. The designed SHIM not only needs to meet the performance requirements of the electromagnetic, but also needs to meet the strength requirements of material for its high-speed rotating condition.

### *4.1. Structure Analysis of Rotor*

Since the rotor is evenly distributed with rotor tooth and rotor slots, it becomes difficult to calculate the rotor stress analytically.

In this paper, the FEM is adopted to analyze and calculate the stress and modal of the rotor. When the rotor speed is 21,000 rpm, its von Mises stress distribution, first-order and second-order bending mode are given in Figure 8. As shown in Figure 8a, the maximum value of von Mises stress occurs at the rounded corner of the connection position between the rotor teeth and the rotor slot, and the value is 447 Mpa. The yield strength of 40 Cr used

for the rotor is 800 Mpa, and the safety factor of the rotor strength under rated operation is calculated to be 1.79. For plastic materials, the safety factor range of its strength is 1.2~2.5; thus, the rotor can operate safely under rated working conditions. In addition, the first- and second-order bending modes of the rotor are given in Figure 8b,c. The corresponding natural frequencies are 753.74 Hz and 1740.8 Hz, respectively. The mechanical frequency corresponding to SHIM at rated speed is 350 Hz, which is lower than 70% of the first-order mode, indicating that the rotor would not have any resonance phenomena at rated operation conditions.

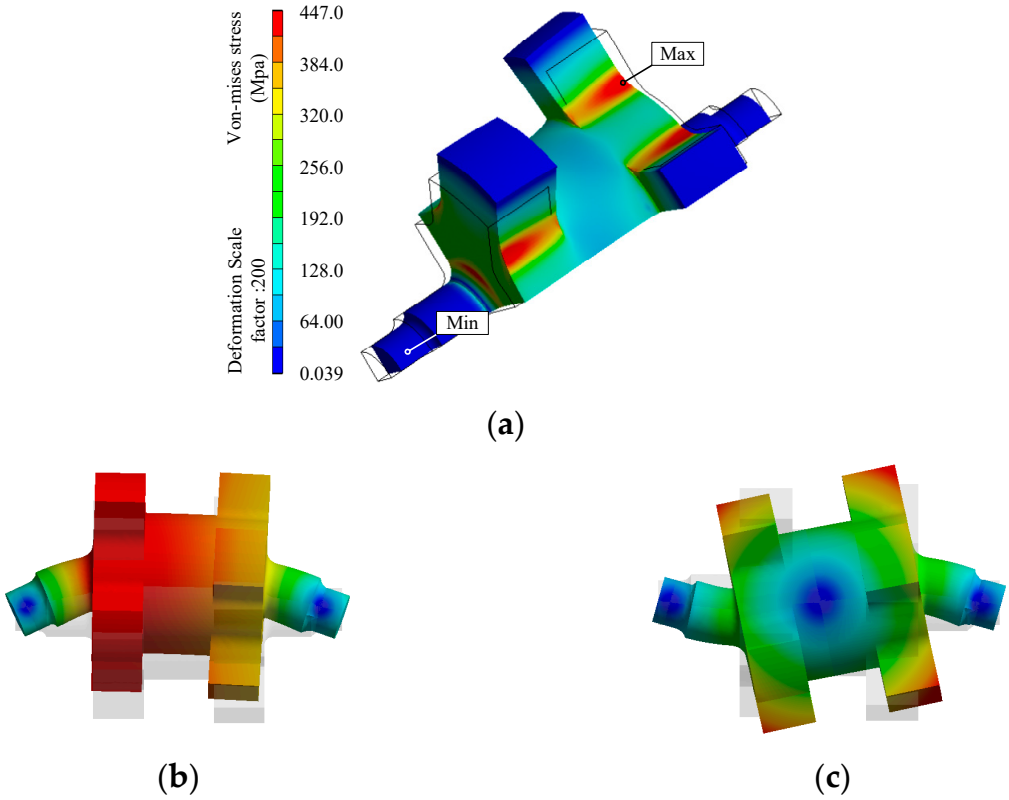



**Figure 8.** Structure analysis and modal analysis of rotor. (**a**) Von mises stress distribution. (**b**) First-order mode (Frequency = 753.74 Hz). (**c**) Second-order mode (Frequency = 1740.8 Hz).

### *4.2. Weight-Saving Design of Rotor*

The mass of the SHIM for all-electric aircraft needs to be reduced as much as possible in order to reduce the total mass of the power supply system and to increase the power density of the SHIM. Based on the results of the previous rotor strength analysis, it is clear that this can be achieved by sacrificing the strength performance of the rotor, subject to safe operation. The original and mass-reduced models of the rotor are shown in Figure 9. The von Mises stress distribution, first-order bending mode and second-order bending mode of the mass-reduced rotor at rated speed are shown in Figure 10. The maximum von Mises stress is 566.2 Mpa, and the corresponding frequencies of the first- and second-order bending modes are 680.91 Hz and 1581.9 Hz, respectively. Compared with the original rotor, the von Mises stress increases by 26.7%, and the frequencies corresponding to the first- and second-order bending modes decrease by 9.7% and 9.1%, respectively. Notably, the strength safety factor of the mass-reduced rotor is 1.41, and its mechanical frequency is still lower than 70% of the first-order natural frequency, indicating that the mass-reduced rotor is still in a safe working state.

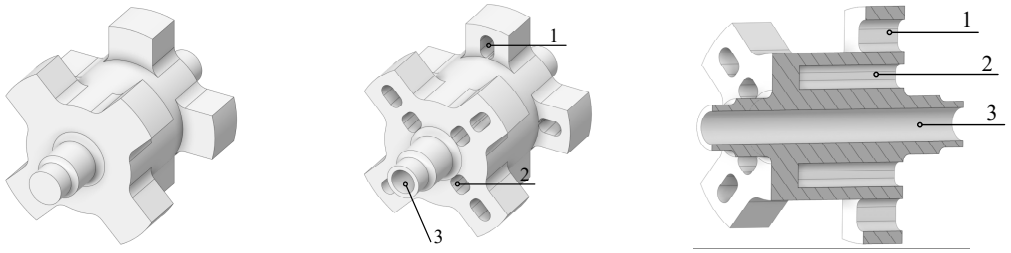



**Figure 9.** Three-dimensional models of the original rotor and the mass-reduced rotor. (**a**) Original rotor. (**b**) Mass-reduced rotor. (**c**) Sectional view of the weight-reduction rotor.

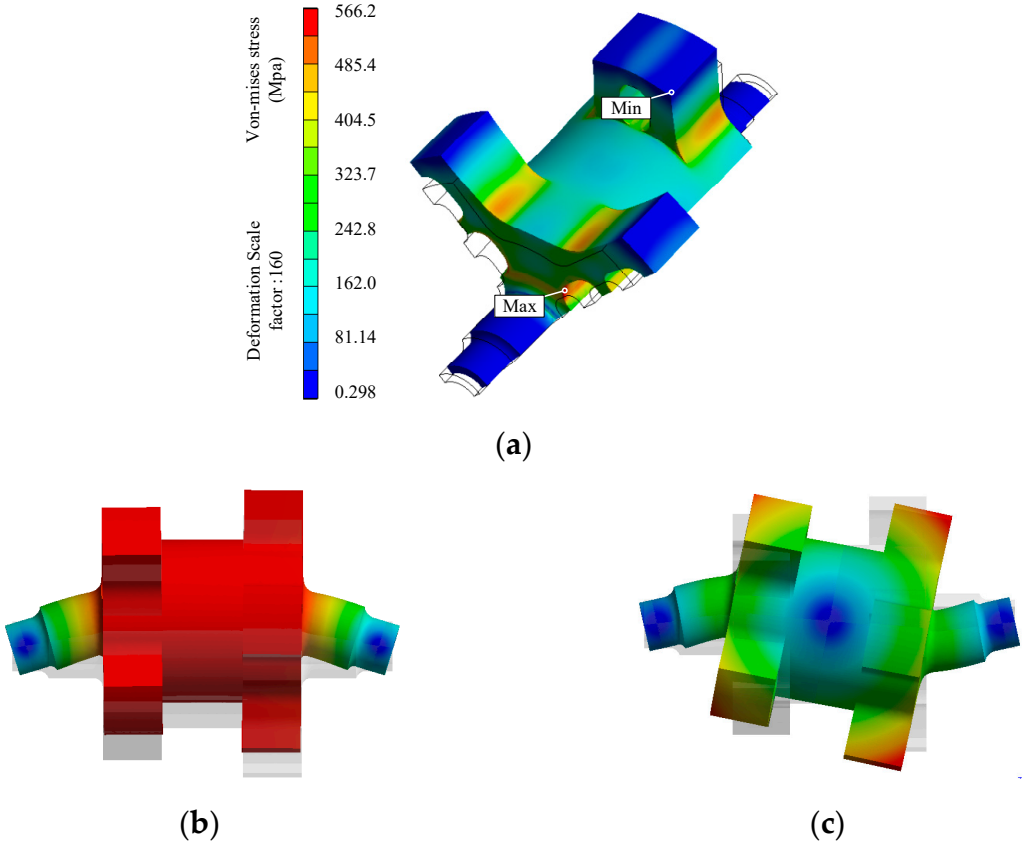
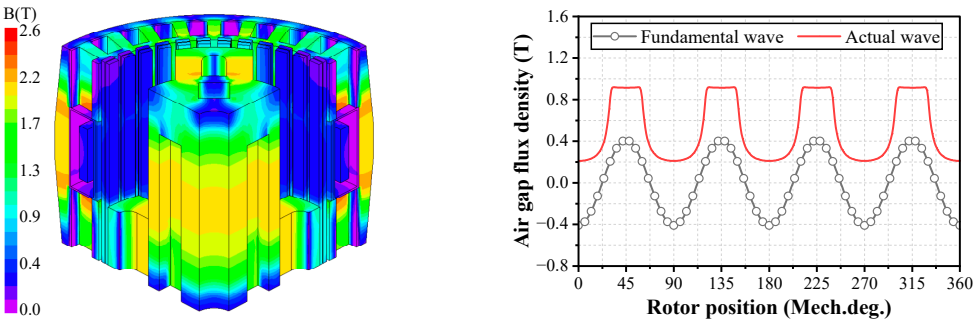



**Figure 10.** Von Mises stress distribution, first-order bending mode and second-order bending mode of the reduced rotor at rated speed. (**a**) Von mises stress distribution. (**b**) First-order bending mode. (**c**) Second-order bending mode.

The mass property comparison between the mass-reduced rotor and the original rotor is shown in Table 3. Compared with the original rotor, the mass of the mass-reduced rotor is reduced by 24.9% and the moment of inertia is reduced by 17.9%. The change in rotor would inevitably lead to the decrease in SHIM output performance at rated state. The no-load flux density distribution of the SHIM with a mass-reduced rotor and the waveform of air-gap flux density are shown in Figure 11. Compared with Figure 4, the flux density of the rotor becomes saturated, and the maximum flux density of the shell is reduced from 2.48 to 2.24 T. In addition, the saturation phenomenon in the mass-reduced rotor leads to the decrease in the amplitude of the air-gap flux density.

**Table 3.** Mass property comparison.

| | Volume ($m^3$) | Mass (kg) | Moment of Inertia ($kg.m^2$) |
|---|---|---|---|
| Original rotor | 0.0085 | 66.56 | 0.4235 |
| Mass-reduced rotor | 0.0064 | 50.02 | 0.3476 |




(**a**) (**b**)

**Figure 11.** The static field magnetic density distribution of the SHIM with mass-reduced rotor and the waveform of air-gap flux density. (**a**) Static field magnetic density distribution. (**b**) Air-gap flux density.

To make the output performance of the SHIM after mass reduction be the same as that before mass reduction, it is necessary to increase the magnetic load or electrical load. According to Figure 11, the middle part of the shell is already in a saturated state, and further increasing the ampere-turns of excitation winding has no obvious effect on increasing the output performance of SHIM. Therefore, the method of increasing electrical load is adopted to improve the torque output capacity of SHIM.

The performance of SHIM before and after mass reduction with the same output power is compared in Table 4. To make the SHIM output the same power, the armature current density of the SHIM with the mass-reduced rotor should be increased while keeping the excitation ampere-turns unchanged. After mass reduction, the efficiency of SHIM is reduced by 0.3%, but its power density is increased by 14.3%. If the electromagnetic load is kept constant, the output power and power density of SHIM decrease after weight reduction. From the point of view of power density, the SHIM with the mass-reduced rotor has significantly better electromagnetic properties.

**Table 4.** Performance comparison.

| | Volume ($m^3$) | Mass (kg) | Moment of Inertia ($kg.m^2$) | Kilowatt Per Kilogram (kW/kg) |
|---|---|---|---|---|
| SHIM with original rotor | 13.0 | 1000 | 97.4 | About 7.1 |
| SHIM with mass-reduced rotor | 13.0 | 788 | 98.5 | About 6.3 |
| SHIM with mass-reduced rotor | 16.5 | 1000 | 97.1 | About 8.0 |

## 5. Conclusions

In this paper, the design and analysis of a superconducting homopolar inductor machine (SHIM) with a power level of one megawatt are carried out. Firstly, to obtain the initial structure parameters of the SHIM, the main dimensional relationships of the SHIM are established. Secondly, the electromagnetic performance of SHIM is analyzed based on the finite element method. Since the slotless structure is adopted, the harmonic content of air-gap flux density and back-EMF are low. The magnetic field acting on superconducting coil is symmetrically distributed. Then, in order to improve the power density of SHIM, a mass-reduced rotor topology is proposed. The mechanical frequence of mass-reduced rotor is lower than 70% of the first-order natural frequency. After the rotor mass is reduced, the magnetic field acting on the superconducting excitation winding can be weakened. In

addition, when the same power is taken as the output target, the power density of the SHIM can be increased by 14.3% after mass reduction.

Although this paper is devoted to the design and analysis of megawatt class SHIM, the method of improving power density in this paper is also applicable to other types of superconducting machines.

**Author Contributions:** Conceptualization and writing—original draft preparation, J.W.; designing and simulation, C.G.; investigation and validation, W.Z.; Writing—review and editing, Q.W. All authors have read and agreed to the published version of the manuscript.

**Funding:** This research was funded by the Natural Science Foundation of Hunan Province (2022JJ30195).

**Data Availability Statement:** Data are contained within the article.

**Conflicts of Interest:** The authors declare no conflicts of interest.

## Nomenclature

| | |
|---|---|
| $m_1$ | Phase number of armature |
| $I$ | Phase current |
| $k_{dp}$ | Winding coefficient |
| $\Phi$ | Magnetic flux per pole |
| $\alpha_\delta$ | Pole arc coefficient |
| $l_{ef}$ | Effective length of armature |
| $A$ | Armature winding line-load |
| $F_{gap}$ | Magnetomotive force |
| $g_{\min}$ | Minimum the airgap length |
| $i_f$ | Excitation current |
| $\Lambda_L$ | Permeability function of left air gap |
| $N_{i,j,k}(\theta)$ | Winding function |
| $E$ | Back EMF |
| $k_{Nm}$ | Waveform factor |
| $f$ | Electric frequence |
| $B_{\max}$ | Maximum value of air-gap flux density |
| $\tau$ | Pole pitch |
| $n$ | Synchronous speed |
| $D$ | Armature diameter |
| $\Lambda_{\max}$ | Maximum of permeability |
| $N_f$ | Number of turns of excitation winding |
| $\mu_0$ | Vacuum permeability |
| $\Lambda_R$ | Permeability function of right air gap |
| $\omega_{mec}$ | Mechanical angular velocity of rotor |

## References

1. Dezhin, D.; Ivanov, N.; Kovalev, K.; Kobzeva, I.; Semenihin, V. System Approach of Usability of HTS Electrical Machines in Future Electric Aircraft. *IEEE Trans. Appl. Supercond.* **2018**, *28*, 1–5. [CrossRef]
2. Zhang, Y.; Cheng, Y.; Qu, R.; Li, D.; Gao, Y.; Wang, Q. AC Loss Analysis and Modular Cryostat Design of a 10-MW High-Temperature Superconducting Double Stator Flux Modulation Machine. *IEEE Trans. Ind. Applicat.* **2022**, *58*, 7153–7162. [CrossRef]
3. Liu, Y.; Ou, J.; Cheng, Y.; Schreiner, F.; Zhang, Y.; Vargas-Llanos, C.; Grilli, F.; Qu, R.; Doppelbauer, M.; Noe, M. Investigation of AC Loss of Superconducting Field Coils in a Double-Stator Superconducting Flux Modulation Generator by Using T-A Formulation Based Finite Element Method. *Supercond. Sci. Technol.* **2021**, *34*, 055009. [CrossRef]
4. Qu, R.; Liu, Y.; Wang, J. Review of Superconducting Generator Topologies for Direct-Drive Wind Turbines. *IEEE Trans. Appl. Supercond.* **2013**, *23*, 5201108. [CrossRef]
5. Chow, C.C.T.; Ainslie, M.D.; Chau, K.T. High Temperature Superconducting Rotating Electrical Machines: An Overview. *Energy Rep.* **2023**, *9*, 1124–1156. [CrossRef]
6. Cheng, M.; Zhu, X.; Wang, Y.; Wang, R.; Wang, W. Effect and Inhibition Method of Armature-Reaction Field on Superconducting Coil in Field-Modulation Superconducting Electrical Machine. *IEEE Trans. Energy Convers.* **2020**, *35*, 279–291. [CrossRef]
7. Li, X.; Liu, S.; Wang, Y. Design and Analysis of a Stator HTS Field-Modulated Machine for Direct-Drive Applications. *IEEE Trans. Appl. Supercond.* **2017**, *27*, 1–5. [CrossRef]

8. Jia, S.; Qu, R.; Li, J.; Fang, H.; Li, D. A Novel Vernier Reluctance Fully Superconducting Direct Drive Synchronous Generator With Concentrated Windings for Wind Power Application. *IEEE Trans. Appl. Supercond.* **2016**, *26*, 1–5. [CrossRef]
9. Sivasubramaniam, K.; Zhang, T.; Lokhandwalla, M.; Laskaris, E.T.; Bray, J.W.; Gerstler, B.; Shah, M.R.; Alexander, J.P. Development of a High Speed HTS Generator for Airborne Applications. *IEEE Trans. Appl. Supercond.* **2009**, *19*, 1656–1661. [CrossRef]
10. Berg, F.; Palmer, J.; Miller, P.; Dodds, G. HTS System and Component Targets for a Distributed Aircraft Propulsion System. *IEEE Trans. Appl. Supercond.* **2017**, *27*, 1–7. [CrossRef]
11. Sivasubramaniam, K.; Laskaris, E.T.; Shah, M.R.; Bray, J.W.; Garrigan, N.R. High-Temperature Superconducting Homopolar Inductor Alternator for Marine Applications. *IEEE Trans. Appl. Supercond.* **2008**, *18*, 1–6. [CrossRef]
12. Lokhandwalla, M.; Haran, K.S.; Alexander, J.P. Scaling Studies of High Speed High Temperature Superconducting Generator. In Proceedings of the 2012 XXth International Conference on Electrical Machines, Marseille, France, 2–5 September 2012; IEEE: Piscataway, NJ, USA, 2012; pp. 751–756.
13. Jeong, J.-S.; An, D.; Hong, J.-P.; Kim, H.-J.; Jo, Y.-S. Design of a 10-MW-Class HTS Homopolar Generator for Wind Turbines. *IEEE Trans. Appl. Supercond.* **2017**, *27*, 1–4. [CrossRef]
14. Kalsi, S.; Hamilton, K.; Buckley, R.; Badcock, R. Superconducting AC Homopolar Machines for High-Speed Applications. *Energies* **2018**, *12*, 86. [CrossRef]
15. Pan, Y.; Yang, J.; Li, Q.; Luo, X.; Huang, S.; Gao, C.; Ma, J. Design of HTS Excitation Coil for Homopolar Inductor Machine Considering Critical Current Reduction of Local Turn. *IEEE Trans. Ind. Appl.* **2024**, 1–9. [CrossRef]
16. Sivasubramaniam, K.; Laskaris, E.T.; Lokhandwalla, M.; Zhang, T.; Bray, J.W.; Gerstler, B.; Shah, M.R.; Alexander, J.P. Development of a High Speed Multi-Megawatt HTS Generator for Airborne Applications. In Proceedings of the 2008 IEEE Power and Energy Society General Meeting—Conversion and Delivery of Electrical Energy in the 21st Century, Pittsburgh, PA, USA, 20–24 July 2008; IEEE: Piscataway, NJ, USA, 2008; pp. 1–4.
17. Li, W.; Chau, K.T.; Ching, T.W.; Wang, Y.; Chen, M. Design of a High-Speed Superconducting Bearingless Machine for Flywheel Energy Storage Systems. *IEEE Trans. Appl. Supercond.* **2015**, *25*, 1–4. [CrossRef]
18. Pan, Y.; Yang, J.; Li, Q.; Huang, S.; Gao, C.; Ma, J. Investigation and Suppression of External Alternating Field of HTS Excitation Coil in Homopolar Inductor Machine. *IEEE Trans. Magn.* **2024**, 1. [CrossRef]
19. Ma, J.; Pan, Y.; Luo, X.; Xiao, H.; Yang, J.; Simpson, N.; Mellor, P. Design of a 10 kW Superconducting Homopolar Inductor Machine Based on HTS REBCO Magnet. *IEEE Trans. Appl. Supercond.* **2024**, *34*, 1–7. [CrossRef]
20. Pan, Y.; Yang, J.; Li, Q.; Luo, X.; Huang, S.; Ma, J. Optimal Design of a High Temperature Superconducting Homopolar Inductor Machine. In Proceedings of the 2023 26th International Conference on Electrical Machines and Systems (ICEMS), Zhuhai, China, 5–8 November 2023; pp. 3920–3925.
21. Dai, S.; Yang, J.; Liu, H.; Feng, Y.; Huang, S. Comparative Study on the Performance of High-Speed IPM Motor with Single-Layer PM for Electric Spindle. In Proceedings of the 2022 IEEE 5th International Electrical and Energy Conference (CIEEC), Nangjing, China, 27–29 May 2022; pp. 963–968.
22. Ye, C.; Yang, J.; Xiong, F.; Zhu, Z.Q. Relationship Between Homopolar Inductor Machine and Wound-Field Synchronous Machine. *IEEE Trans. Ind. Electron.* **2020**, *67*, 919–930. [CrossRef]
23. Lou, Z.; Yu, K.; Wang, L.; Ren, Z.; Ye, C. Two-Reaction Theory of Homopolar Inductor Alternator. *IEEE Trans. Energy Convers.* **2010**, *25*, 677–679. [CrossRef]
24. Li, Q.; Yang, J.; Huang, S.; Liu, P.; Feng, Y.; Wang, L. No-Load Electromagnetic Performance Analysis of a Mechanically Modulated Permanent Magnet Homopolar Inductor Machine. *IEEE Trans. Transp. Electrif.* **2022**, *8*, 1168–1181. [CrossRef]
25. Yang, J.; Ye, C.; Huang, S.; Li, Y.; Xiong, F.; Zhou, Y.; Xu, W. Analysis of the Electromagnetic Performance of Homopolar Inductor Machine Through Nonlinear Magnetic Equivalent Circuit and Air-Gap Permeance Function. *IEEE Trans. Ind. Appl.* **2020**, *56*, 267–276. [CrossRef]
26. Yang, J.; Liu, P.; Ye, C.; Wang, L.; Zhang, X.; Huang, S. Multidisciplinary Design of High-Speed Solid Rotor Homopolar Inductor Machine for Flywheel Energy Storage System. *IEEE Trans. Transp. Electrific.* **2021**, *7*, 485–496. [CrossRef]
27. Krings, A.; Cossale, M.; Tenconi, A.; Soulard, J.; Cavagnino, A.; Boglietti, A. Magnetic Materials Used in Electrical Machines: A Comparison and Selection Guide for Early Machine Design. *IEEE Ind. Appl. Mag.* **2017**, *23*, 21–28. [CrossRef]


**Disclaimer/Publisher's Note:** The statements, opinions and data contained in all publications are solely those of the individual author(s) and contributor(s) and not of MDPI and/or the editor(s). MDPI and/or the editor(s) disclaim responsibility for any injury to people or property resulting from any ideas, methods, instructions or products referred to in the content.